ISSN (Print) 1226-1750
ISSN (Online) 2233-6656
Journal of Magnetics 31(3), 275-289 (2026) https://doi.org/10.4283/JMAG.2026.31.3.275

A 2-D Electromagnetic Analysis Method for 2-Pole/8-Slot Bearingless Motors Considering Axial and Radial Flux Leakage Effects

Hyung-Il Park[1] and Min-Mo Koo[2]*

[1]*Department of Convergence Technology Laboratory, Korea Electric Power Research Institute, Daejeon 34056, Republic of Korea*
[2]*Department of Purpose-Built Mobility Group, Korea Institute of Industrial Technology, Gwangju 61012, Republic of Korea*

(Received 19 August 2026, Received in final form 4 September 2026, Accepted 8 September 2026)

Recently, bearingless motors (BLMs) have attracted significant attention for high-purity pump applications due to their non-contact operation, which eliminates mechanical wear and contamination. However, to achieve a compact footprint, BLMs often employ a thin disk-type rotor and a stator with bent-teeth topology. This specialized structure inherently induces severe axial and radial end flux leakages, as well as fringing flux, which cannot be accurately predicted using conventional two-dimensional (2-D) finite element analysis (FEA). Although three-dimensional (3-D) FEA provides high accuracy, its heavy computational cost limits its utility during initial design optimization. To resolve this trade-off, this paper proposes a modified permeability-based 2-D equivalent analysis method for BLMs that comprehensively accounts for both axial and radial flux leakage pathways. By formulating equivalent permeability correction factors from 3-D magnetic flux distributions, the proposed method effectively maps complex 3-D leakage behaviors into a computationally efficient 2-D domain. The validity and generality of the proposed model are rigorously verified through comparative evaluations across key dimensional ratios. The proposed approach maintains 3-D FEA-level precision while drastically reducing computation time and resource consumption, offering a highly practical tool for early-stage BLM design.

Keywords : bearingless motor, 2-D equivalent analysis, leakage flux, permeance factor

1. Introduction

Recently, there has been a rapidly increasing demand for pump systems capable of high-cleanliness, high-precision, and highly reliable operation, particularly in industries such as semiconductor manufacturing, bio-pharmaceuticals, fine chemicals, and medical devices. In these sensitive applications, conventional mechanical bearings pose significant challenges, as lubricant contamination or particle wear resulting from contact between the rotor and the bearing can lead to process failures or product damage. Furthermore, pumps based on mechanical bearings suffer from inherent limitations, including friction-induced heat generation, performance degradation due to mechanical wear, and complex maintenance requirements, rendering them unsuitable for high-purity environments [1-7].

To address these limitations, bearingless motors (BLMs) have emerged as a promising alternative, attracting significant attention across various high-end industries for their ability to achieve non-contact rotation through electromagnetic levitation. BLMs function as an integrated electromagnetic drive system that simultaneously generates driving torque and maintains magnetic suspension of the rotor, eliminating the need for additional mechanical bearing systems. Consequently, BLMs are free from mechanical losses and friction-related wear, require no lubricants, ensure long-term operational stability, and significantly reduce maintenance burdens. In particular, the disk-type rotor structure commonly adopted in BLMs allows for passive magnetic stabilization in both tilting and axial directions. This passive stabilization effectively reduces the complexity of the control system while ensuring stable operation under high-speed conditions. Furthermore, the structural simplicity of BLMs offers distinct advantages in terms of miniaturization and weight reduction, making them an ideal solution for applications where high cleanliness and high reliability are paramount.

©The Korean Magnetics Society. All rights reserved.
*Corresponding author: Tel: +82-62-600-6230
Fax: +82-62-600-6219, E-mail: mmkoo@kitech.re.kr

© 2026 Journal of Magnetics

To realize a compact physical footprint, BLMs often incorporate a stator structure with bent teeth, effectively minimizing the overall radial dimensions. However, this thin and flat structural topology inherently induces significant axial flux leakage. Furthermore, the specialized geometry of the bent teeth promotes prominent radial flux leakage as well. Consequently, the performance characteristics of BLMs are strongly governed by complex three-dimensional (3-D) flux pathways, including both axial and radial end leakage fluxes as well as fringing flux.

Because conventional two-dimensional (2-D) Finite Element Analysis (FEA) cannot account for these inherently 3-D flux leakages, its predictive accuracy for electromagnetic performance is fundamentally limited. Therefore, 3-D FEA has traditionally been regarded as essential for the precise electromagnetic characterization and design of BLMs. However, 3-D FEA involves high computational complexity and excessive consumption of computing resources. This poses a major bottleneck during the initial design phase, where iterative simulations across numerous design parameters are required. Particularly in the conceptual design stage—which entails continuous structural comparisons and sensitivity analyses—the severe time consumption of 3-D FEA significantly delays the overall optimization process, leading to substantial engineering inefficiency. In electric motors requiring 3-D analysis, the flux leakages occurring at the rotor and stator ends account for a non-negligible portion of the total magnetic flux. Neglecting these end-leakage effects causes 2-D FEA-based performance predictions to deviate significantly from 3-D FEA or experimental validation results. To overcome this issue, recent studies have actively focused on incorporating axial leakage and fringing effects into 2-D FEA, particularly for permanent magnet synchronous motors (PMSMs). Chen *et al.* analyzed the impact of flux leakage on a limited scale using a lumped-parameter magnetic equivalent circuit (LPMC) model for permanent magnet motors. Furthermore, Jung et al. and Lee et al. proposed analytical techniques that adjust the magnetic permeability in the 2-D domain based on theoretical flux path modeling to account for axial leakage paths. These hybrid approaches have attracted considerable attention as they effectively strike a balance between the high computational efficiency of conventional 2-D simulations and the precise accuracy of 3-D FEA [8-13].

However, existing literature has predominantly focused on standard PMSMs to compensate solely for axial flux leakage. Unlike conventional PMSMs, the target BLM in this study features a specialized topology combining a thin, disk-type structure with bent stator teeth, where both axial and radial flux leakages naturally co-occur. To address this issue, this paper proposes a modified permeability-based 2-D equivalent analysis model that comprehensively accounts for both axial and radial end flux paths. By analyzing the 3-D leakage paths at the stator and rotor ends, correction factors are derived to accurately map the 3-D flux distribution into a computationally efficient 2-D FEA model. Furthermore, to verify the generality and reliability of the proposed method, comparative analyses are conducted across various dimensional ratios, including the outer diameter-to-stack length ratio and the tooth width-to-tooth thickness ratio. The proposed approach significantly reduces computation time and resource consumption while maintaining 3-D FEA-level accuracy, making it highly effective for iterative evaluations and sensitivity analyses during the preliminary design stage of 2-pole/8-slot BLMs.

2. Proposed 2-D Analysis Method Considering Axial and Radial Flux Leakage

2.1. Analysis Model

The BLM evaluated in this study features a disk-type rotor structure capable of simultaneously achieving passive magnetic levitation and driving torque, as illustrated in Fig. 1. The analytical model of the BLM comprises a permanent magnet (PM) rotor, a stator core, motor drive coils, and suspension coils. The rotor consists of a hollow ring-shaped permanent magnet, while the stator incorporates a specialized bent-teeth topology to minimize overall radial dimensions. The target model is configured as a two-phase BLM with a 2-pole, 8-slot structure, where both the drive and suspension coils are wound around the bent stator teeth. To provide a clear structural understanding of this specialized topology and its winding

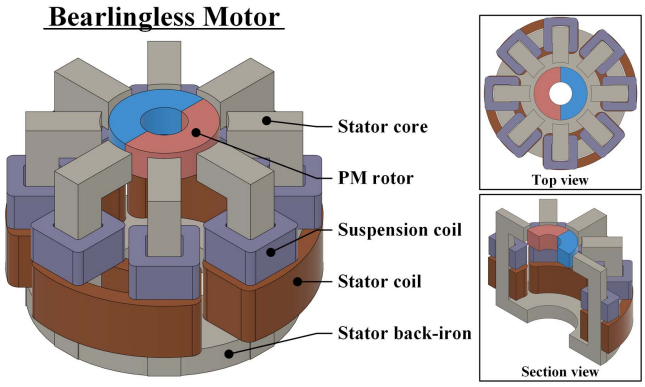


Fig. 1. (Color online) Structure and 3-D analysis model of the target BLM.

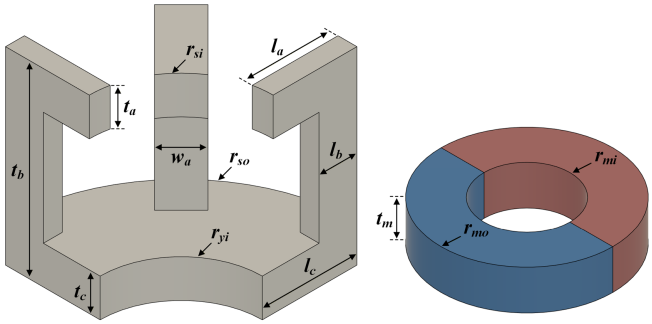


Fig. 2. (Color online) Dimensional parameters of the target BLM: (a) stator core, (b) rotor magnet.

Table 1. Specifications and dimensional parameters of the 2-pole/8-slot BLM.

Parameter	Value	Parameter	Value
pole	2 pole	*slot* (N_s)	8 slot
r_{so}	42.5 mm	l_a	24 mm
r_{si}	18.5 mm	l_b	11 mm
r_{yi}	15 mm	l_c	27.5 mm
r_{mo}	15 mm	*air gap*	3.5 mm
r_{mi}	5.5 mm	k_a	4
t_a (L_{st})	11 mm	k_r	10
t_b	60 mm	B_r	1.0 T
t_c	10 mm	N_t (*turns per coil*)	80
t_m	11 mm	*rated current*	6 A
w_a	11 mm	*max current*	10 A

layout, both the top view and section view are presented in Fig. 1, schematically illustrating the overall geometry and magnetic flux paths. Furthermore, Fig. 2 illustrates the detailed dimensional parameters of the stator and rotor cores, and Table 1 summarizes the primary geometric specifications and design parameters of the target motor.

2.2. 3-D Magnetic Field Distribution and Flux Leakage Effects

The magnetic flux pathways in BLM exhibit highly complex 3-D behaviors owing to the end geometries of the rotor and stator, the air-gap configuration, and the winding layout. In particular, significant end-leakage and fringing fluxes occur along both the axial and radial directions. To characterize these 3-D flux pathways, this study evaluated the magnetic flux density distributions under no-load and loaded conditions using 3-D FEA.

Figs. 3 and 4 show the magnetic flux density and leakage flux distributions on the *r-z* cross-sectional plane surrounding the motor under no-load and loaded conditions, respectively. Under the no-load condition, a substantial portion of the magnetic flux generated by the permanent magnets fails to link with the stator, resulting in prominent leakage into the surrounding air near the internal region and axial end portions of the rotor. Conversely, under the loaded condition, the drive currents induce higher magnetic saturation in the stator teeth and yoke, which expands the spatial extent of both axial and radial flux leakages. To examine the leakage flux behavior in greater detail, the leakage flux distributions were evaluated along the radial position surrounding the motor, as shown in Figs. 5 and 6. Under the no-load condition, high leakage flux levels are concentrated near the magnets and along the axial direction of the stator teeth. Under the loaded condition, significant axial flux leakage extends even to the bent sections of the stator teeth. Furthermore, Fig. 7 illustrates the radial flux leakage generated around the stator. Due to the specialized bent-

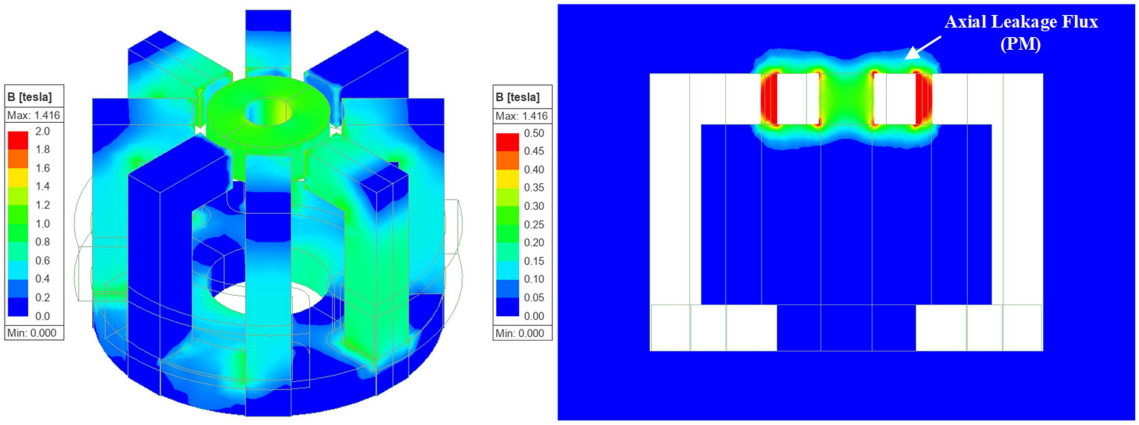


Fig. 3. (Color online) Magnetic flux density and leakage flux distribution on the *r-z* plane under no-load condition.

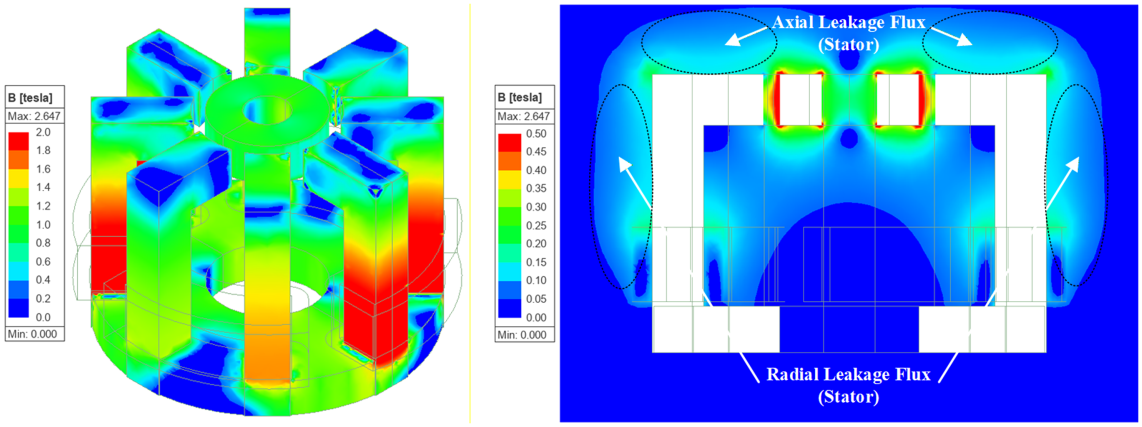


Fig. 4. (Color online) Magnetic flux density and leakage flux distribution on the *r-z* plane under load condition.

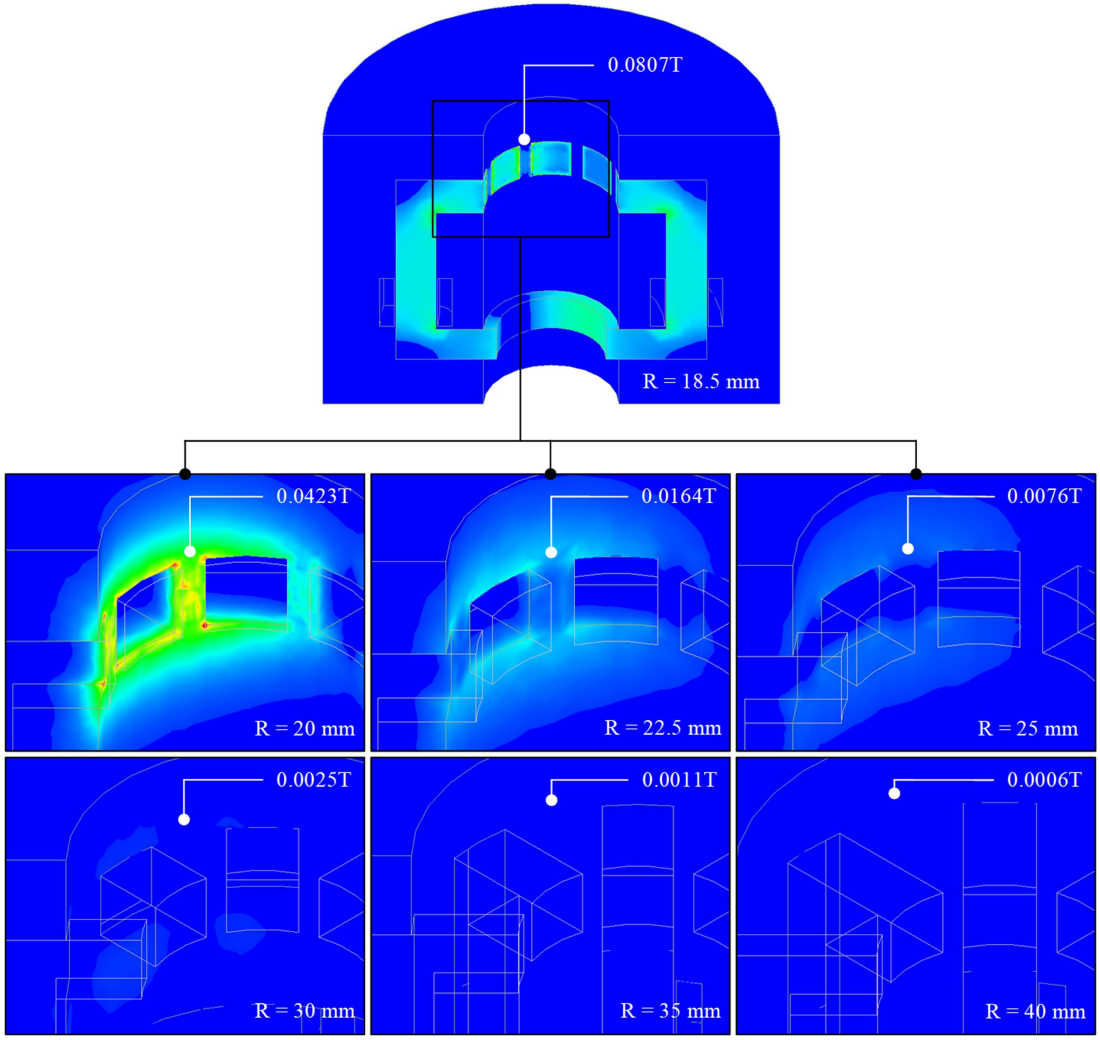


Fig. 5. (Color online) Leakage flux distribution along the radial position under no-load condition.

teeth topology, noticeable leakage fluxes are observed around the stator teeth depending on the axial position.

The extensive distribution of leakage fluxes around the rotor magnet and stator periphery confirms that this specialized topology cannot be accurately modeled using conventional 2-D FEA alone. Consequently, these findings

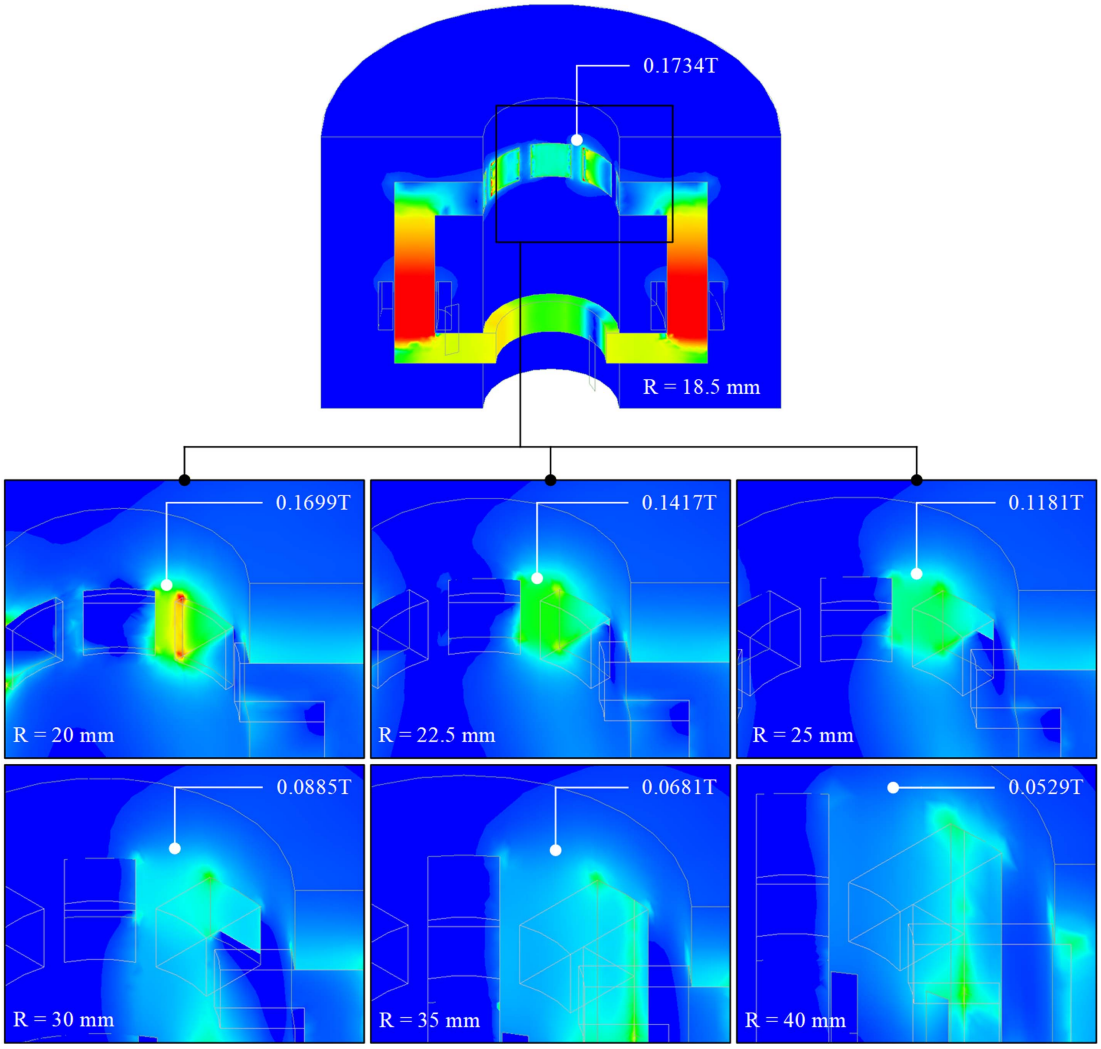


Fig. 6. (Color online) Leakage flux distribution along the radial position under load condition.

highlight the necessity of proposing a modified 2-D analysis model that incorporates the complex 3-D leakage flux pathways.

2.3. Flux Leakage Path Modeling Considering Axial and Radial Flux Leakage

Based on the previously analyzed 3-D magnetic field distribution and flux leakage behaviors, the axial and radial flux leakage pathways can be analytically modeled. Fig. 8 illustrates the magnetic flux path modeling divided into four distinct regions based on the cross-sectional geometry of the stator core. To establish the 2-D equivalent model of the BLM, the permeances and permeance coefficients considering both the main flux and leakage flux components within each of the four regions are derived [8-13]. The permeances accounting for the axial and radial leakage paths occurring around the stator teeth can be expressed as shown in Equations. (1)–(5):

$$P_{mk}^{a,r,m} = \mu_0 \frac{H_k^{a,r,m}}{W_{ok}^{a,r,m}} L_{st} \tag{1}$$

$$P_{sk}^{a,r,m} = 0.264 \mu_0 H_k^{a,r,m} \tag{2}$$

$$P_{tk}^{a,r} = \mu_0 \frac{(W_{sk}^{a,r} - W_{ok}^{a,r})}{\pi W_{sk}^{a,r}} H_k^{a,r} \tag{3}$$

$$P_{ei} = 0.77 \mu_0 W_{ok}^{a} \tag{4}$$

$$P_{eo} = 0.125 \mu_0 (\pi r_{so} - W_{ok}^{a}) \tag{5}$$

Here, the subscripts *a*, *r*, *m*, *ei* and *eo* denote the axial leakage effect prior to tooth bending, the radial leakage effect after tooth bending, the flux leakage toward the permanent magnet, and the leakage effects at the inner

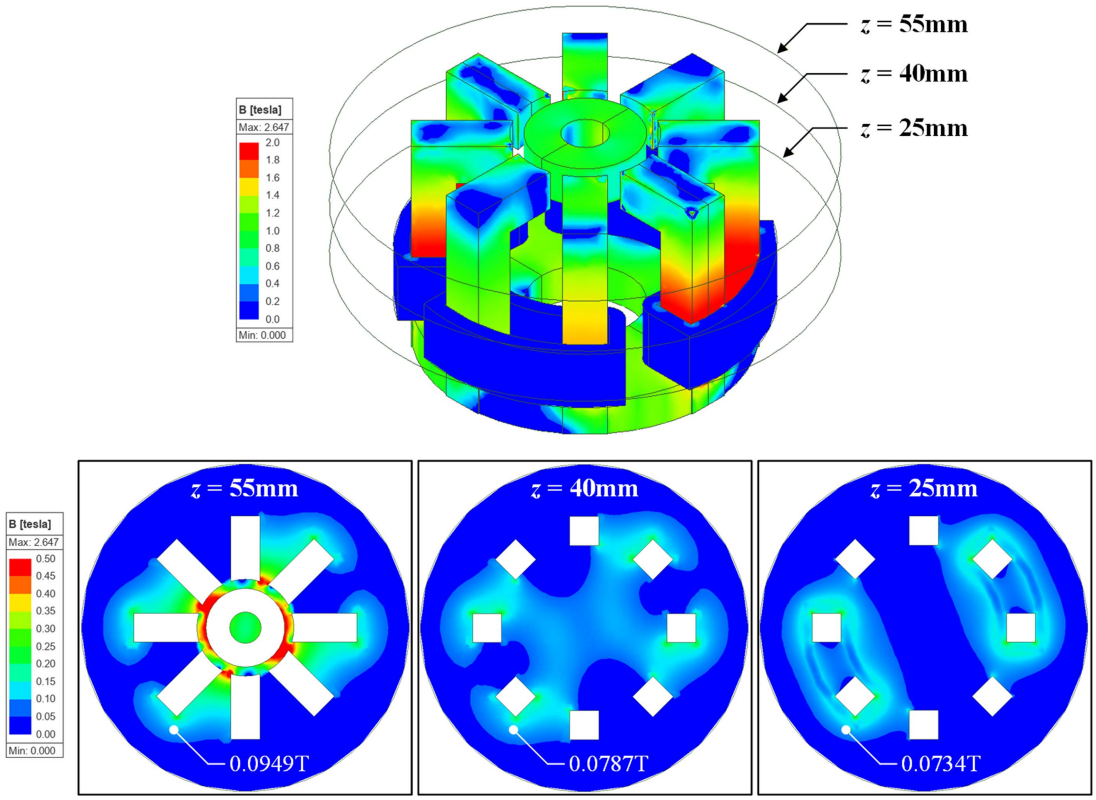


Fig. 7. (Color online) Leakage flux distribution along the axial position of the stator core under load condition.

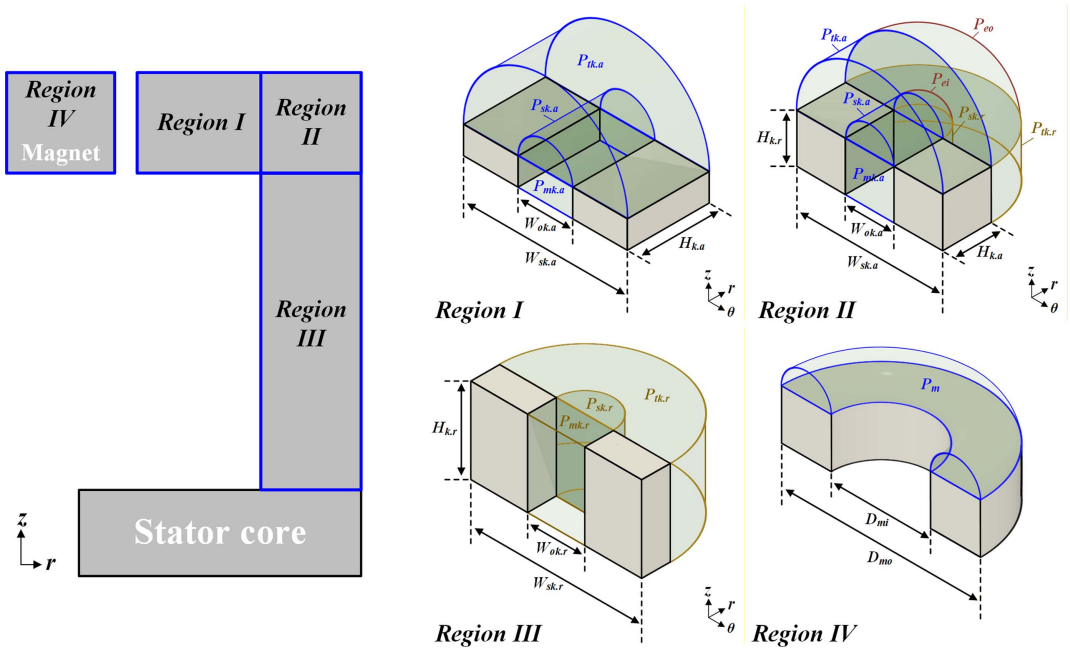


Fig. 8. (Color online) Region division and magnetic flux path modeling of the BLMs.

and outer edges of the bent section, respectively. The parameters μ_0, L_{st}, and r_{so} represent the permeability of vacuum, the axial stack length, and the outer radius of the BLM stator, respectively. Furthermore, H_k, W_{ok}, and W_{sk} denote the average height, the average slot width, and the average tooth pitch used to calculate the permeance

factors in each region, where the subscript k indicates the specific sub-region index of the discretized 2-D equivalent model. The explicit formulations for these parameters are summarized in the Appendix.

By formulating the derived permeances into corrected permeance factors for the axial, radial, and edge regions of the stator, as well as the axial region of the rotor permanent magnet, the corresponding expressions are obtained as shown in Eqs. (6)–(10):

$$\mu_{rk}^{I} = \frac{P_{mk\,mk.a}^{a} + 2(P_{sk}^{a} + P_{tk}^{a})}{P_{mk}^{a}} \tag{6}$$

$$\mu_{rk}^{II.a} = \frac{P_{mk}^{a} + P_{sk}^{a} + P_{tk}^{a} + 0.5(P_{eo} + P_{ei})}{P_{mk}^{a}} \tag{7}$$

$$\mu_{rk}^{II.r} = \frac{P_{mk}^{r} + P_{sk}^{r} + P_{tk}^{r} + 0.5(P_{eo} + P_{ei})}{P_{mk}^{r}} \tag{8}$$

$$\mu_{rk}^{III} = \frac{P_{mk}^{r(r_c)} + P_{sk}^{r(r_i)} + P_{sk}^{r(r_o)} + P_{tk}^{r(r_i)} + P_{tk}^{r(r_o)})}{P_{mk}^{r(r_c)}} \left[1 + \frac{k(k+\alpha)}{2r_c} H_k^{r(r_c)}\right] \tag{9}$$

$$\mu_{rk}^{IV} = \frac{P_{mk}^{m} + 2P_{sk}^{m}}{P_{mk}^{m}} \tag{10}$$

Here, r_i and r_o denote the inner and outer radii of each calculation region, respectively, and $r_c = (r_i + r_o)/2$ represents the mean radius. The parameter α denotes the radial length of the effective area within the slot. Eq. (9) expresses the permeance factor considering the radial flux leakage effect in Region III. To numerically compensate for the increased radial slot length in the 2-D equivalent model, a correction for the radial slot length was incorporated into the formulation.

2.4. Proposed 2-D Equivalent Analysis Model

Fig. 9 illustrates the 2-D equivalent analysis model of the target BLM, constructed by incorporating the magnetic flux path analysis and permeance factors derived in Sections 2.2 and 2.3. The target motor is fundamentally categorized into four main domains based on the 3-D axial and radial flux leakage paths shown in Fig. 8. In the proposed 2-D equivalent model, the stator slot area is classified into three main regions, which are further subdivided into 14 distinct sub-regions to apply specific permeance factors. This regional discretization is defined based on magnetic flux path characteristics to effectively account for structural features, such as the bent-teeth topology of the stator and the coil layout. Additionally, the PM rotor is incorporated into the analytical model as the 15th region. It should be noted that while 15 sub-regions are defined here as a representative baseline to demonstrate the methodology, the number of sub-regions can be flexibly configured depending on the required analytical precision without altering the underlying four-domain flux path framework. The stator core dimensions in the 2-D equivalent model are configured to accurately reflect the 3-D FEA geometry, and the explicit formulations determining these equivalent dimensions are summarized in the Appendix.

3. Analysis Results and Comparative Validation according to Dimensional Ratios

Table 2 summarizes the derived permeance factors for the proposed 2-D equivalent analysis model of the BLM in Table 1. To verify the predictive accuracy and reliability of the proposed method, comparative evaluations were conducted among conventional 2-D FEA, 3-D FEA, and

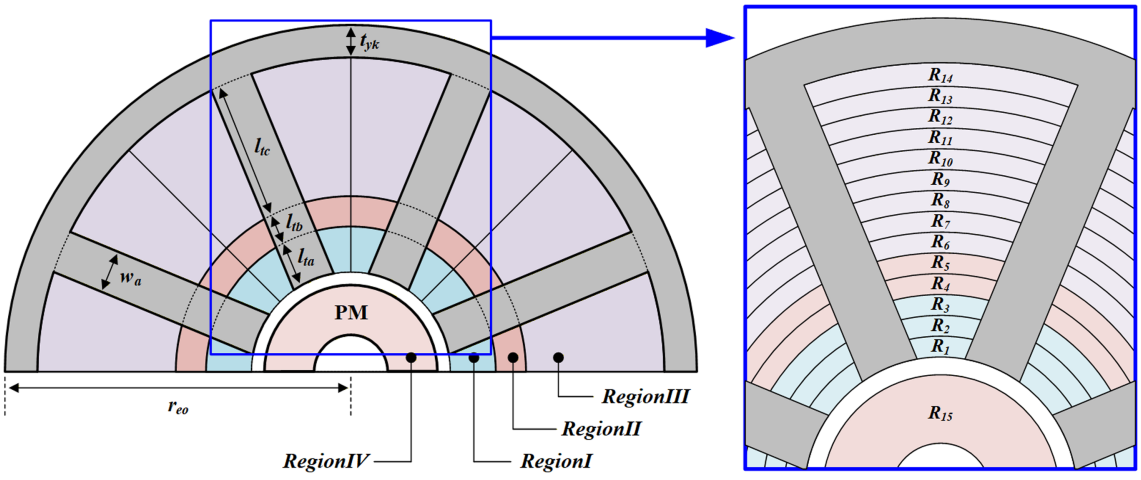


Fig. 9. (Color online) 2-D equivalent analysis model of the BLMs for FEA.

Table 2. Permeance factors of the 2-pole/8-slot BLM.

Region	Factor (μ_r)	Region	Factor (μ_r)	Region	Factor (μ_r)
R_1	1.4558	R_6	2.8948	R_{11}	4.2332
R_2	1.7123	R_7	3.1625	R_{12}	4.5009
R_3	1.9426	R_8	3.4302	R_{13}	4.7686
R_4	2.1575	R_9	3.6979	R_{14}	5.0364
R_5	2.6272	R_{10}	3.9656	R_{15}	1.4320

the proposed 2-D equivalent FEA model incorporating the region-specific permeance factors. All finite element simulations were performed using Ansys Electronics Desktop 2026 R1.

3.1. Analysis Results under No-load and Load Conditions

Figs. 10 and 11 illustrate the magnetic field distribution results under no-load and loaded conditions, respectively, comparing the conventional 2-D model and the proposed 2-D equivalent model incorporating the corrected permeance factors. Under the no-load condition, a noticeable reduction in magnetic flux density within the hollow-core region of the rotor magnet is observed in the proposed 2-D model, effectively reflecting the 3-D flux leakage behavior. Under the loaded condition, the leakage effect inside the slot regions increases due to the adjusted relative permeability. This leakage flux serves as a critical governing factor that directly influences both the magnitude and waveform profile of the electromagnetic torque during loaded operation.

Figs. 12 and 13 present the back-EMF analysis results

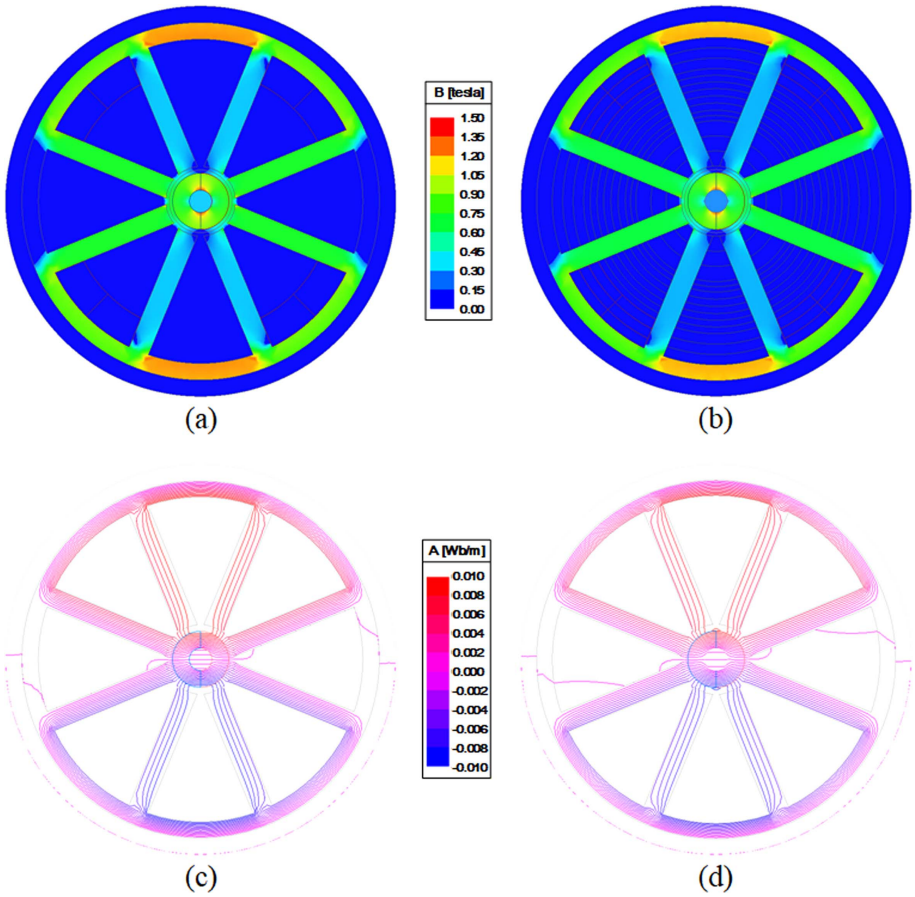


Fig. 10. (Color online) Magnetic flux density distributions under no-load condition: (a) flux density without permeance factors, (b) flux density with permeance factors, (c) flux line without permeance factors, (d) flux line with permeance factors.

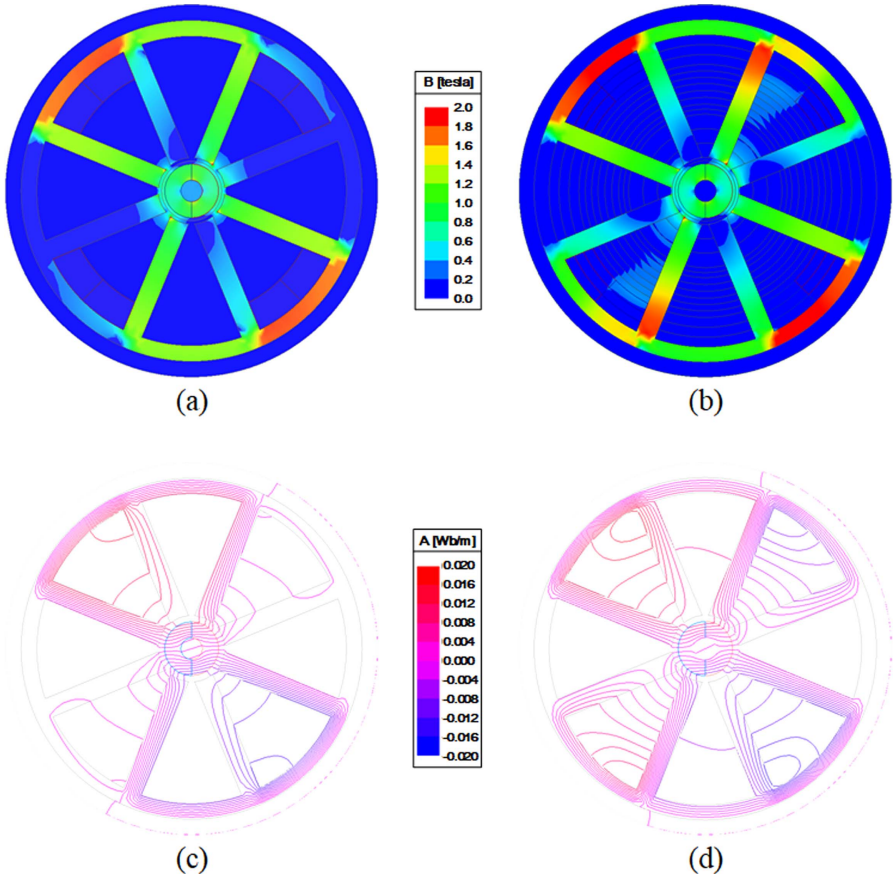


Fig. 11. (Color online) Magnetic flux density distributions under load condition: (a) flux density without permeance factors, (b) flux density with permeance factors, (c) flux line without permeance factors, (d) flux line with permeance factors.

of the target motor under the no-load condition. Because the proposed 2-D analysis method effectively incorporates the flux leakage effects around the permanent magnet, a noticeable reduction in the back-EMF magnitude is observed compared to the conventional method. Furthermore, when evaluated against the 3-D FEA results as a benchmark, the conventional 2-D method yields an analysis error of 8.68%. In contrast, the proposed 2-D equivalent method significantly improves accuracy, achieving an error of only 1.42%.

Figs. 14 and 15 present the electromagnetic torque analysis results of the target motor under various load current conditions. Compared to the 3-D FEA benchmark, the conventional 2-D method exhibits significant discrepancies in both torque magnitude and waveform profile. In contrast, the proposed 2-D equivalent method demonstrates strong agreement with the 3-D FEA results across both magnitude and wave shape. Furthermore, as depicted in Fig. 15, when evaluating the over-current region exceeding the maximum design current ($I > 16A$)—which also serves to reflect the increased stator magnetic saturation level under dual drive and suspension excitation—the average torque calculated by the proposed method remains highly consistent with 3-D FEA. However, an increase in the relative error for torque ripple is observed in this region. This discrepancy in torque ripple stems from localized magnetic saturation differences in the stator yoke. Although this localized saturation effect presents an area for future model refinement, this high-current regime lies outside the normal operational and design range of the target motor. Table 3 summarizes the analysis results of the average torque and torque ripple. Table 4 shows the comparison of computation time and number of mesh elements for each analysis method. To evaluate the electromagnetic torque at a single analysis point, simulations were performed on a workstation equipped with an Intel Core Ultra 9 185H processor (2.3 GHz) and 64.0 GB RAM. The 2-D and 3-D FEA were conducted based on the same step time. To balance computational cost and solution precision, the mesh refinement criteria were configured with energy error rate thresholds below 0.1% for the 2-D FEA and below 0.5% for the 3-D FEA, respectively. While the 3-D FEA took approximately 3,186 seconds, the proposed 2-D FEA

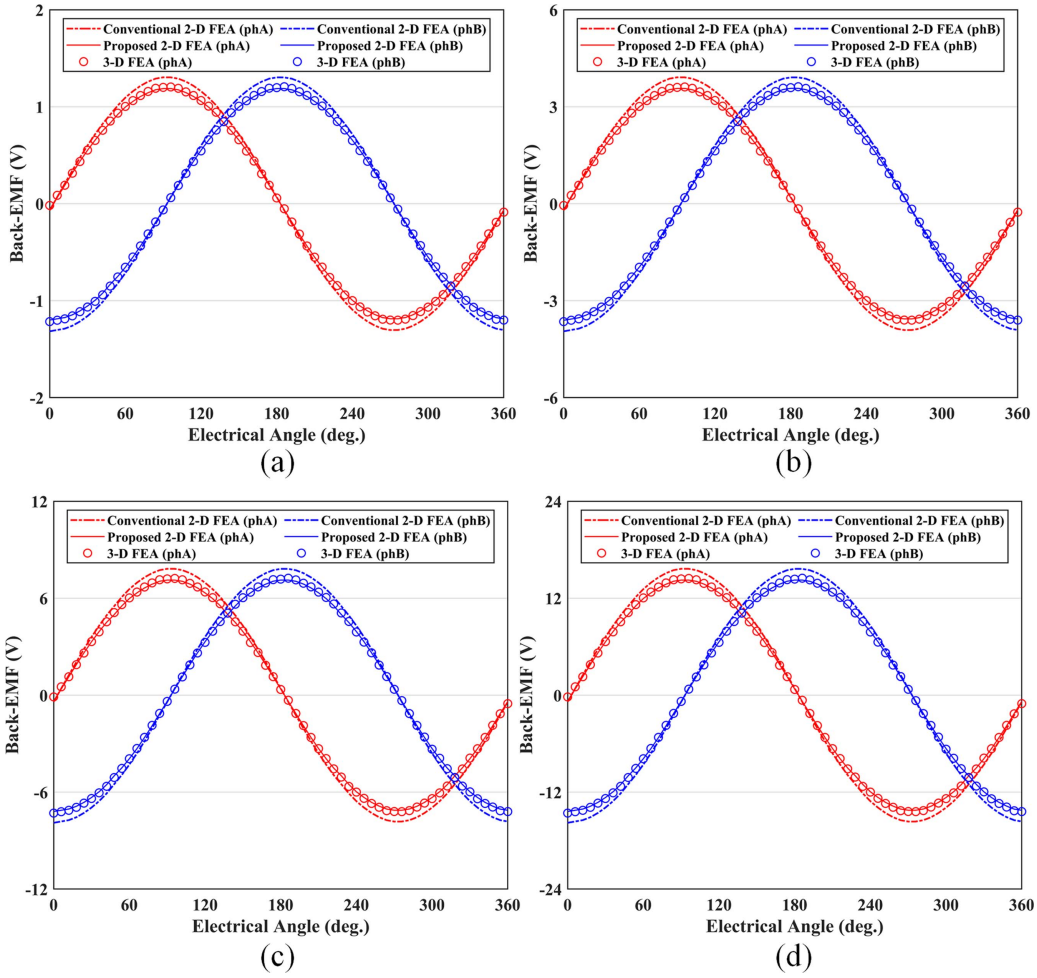


Fig. 12. (Color online) No-load back-EMF waveforms under rotational speed conditions: (a) 500 rpm, (b) 1500 rpm, (c) 3000 rpm, (d) 6000 rpm.

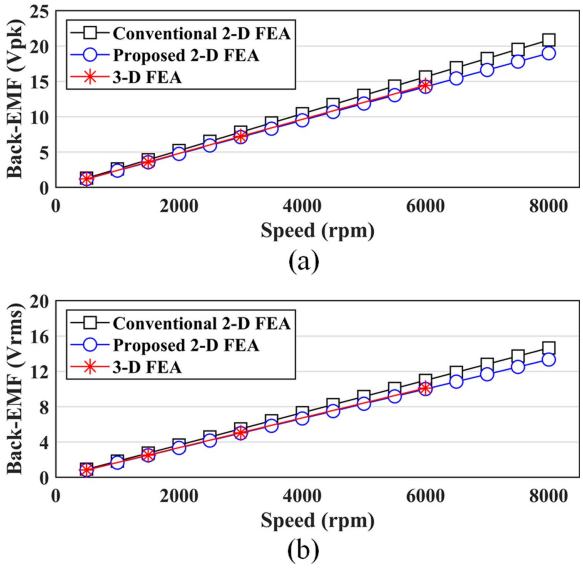


Fig. 13. (Color online) Comparison of no-load back-EMF according to rotational speed: (a) peak value, (b) RMS value.

completed the calculation in just 9 seconds. This demonstrates a significant reduction in computation time of approximately 99.7%.

3.2. Comparative Validation according to Dimensional Ratios

To further validate the reliability and general applicability of the proposed 2-D equivalent analysis method, parametric evaluations were conducted by varying key structural dimension ratios of the BLM. Specifically, the sensitivity analysis was performed considering two primary aspect ratios: the outer diameter-to-stack length ratio (D_{so}/L_{st}) of the motor, and the width-to-thickness ratio (W_a/T_a) of the stator teeth.

Fig. 16 illustrates the geometric configurations established to evaluate motor performance across various outer diameter (D) and stack length (L) proportions of the target BLM. Table 5 summarizes the specific dimensional

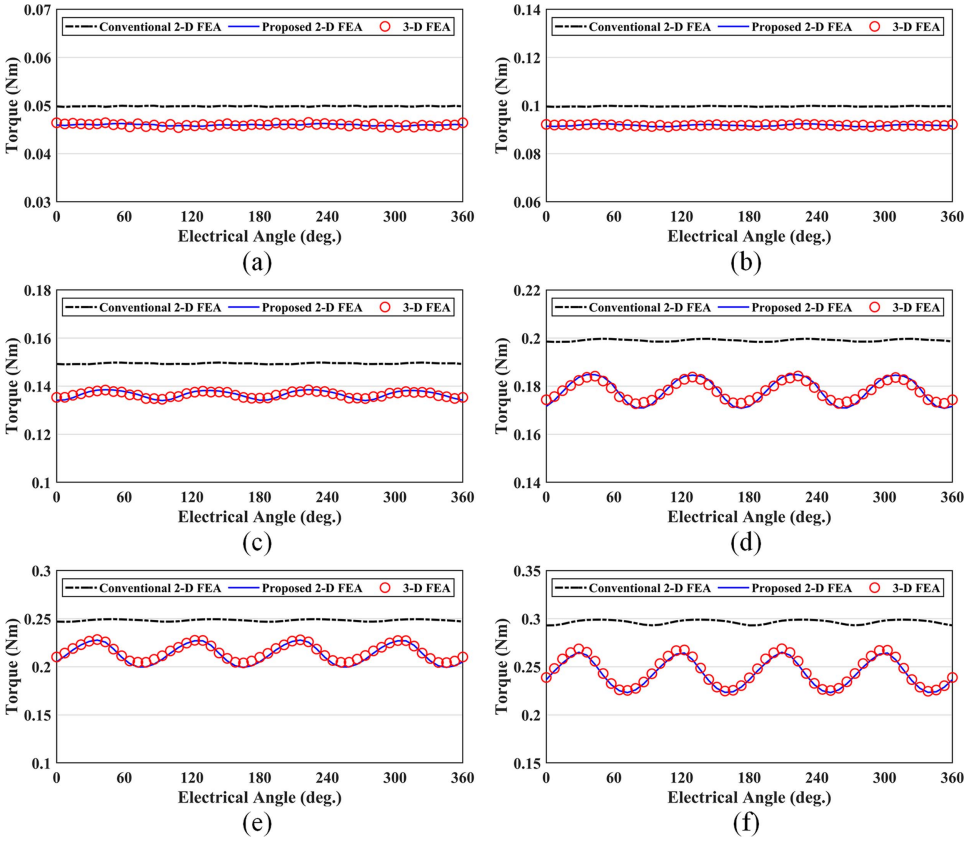


Fig. 14. (Color online) Electromagnetic torque waveforms under load conditions: (a) I = 2 A, (b) I = 4 A, (c) I = 6 A, (d) I = 8 A, (e) I = 10 A, (f) I = 12 A.

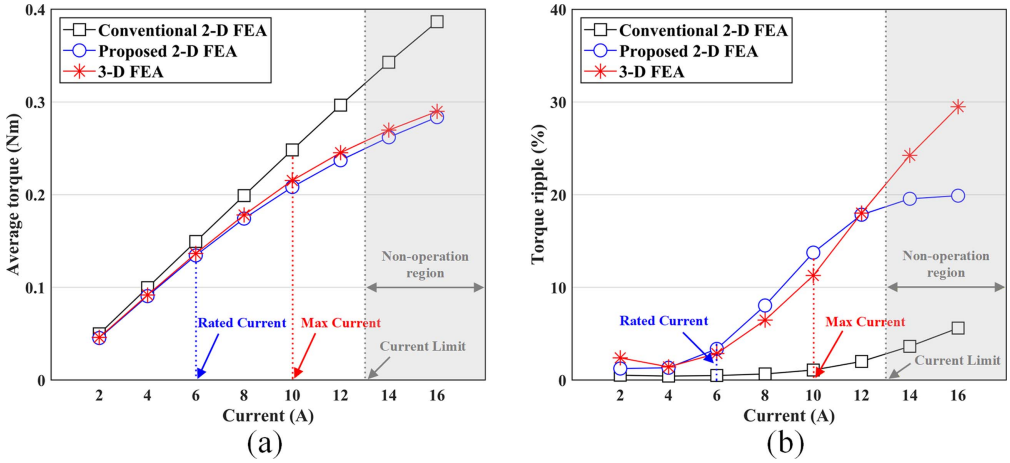


Fig. 15. (Color online) Average torque and torque ripple characteristics as a function of load currents: (a) average torque, (b) torque ripple.

Table 3. Electromagnetic torque under load currents.

Specification		Value		
		3-D FEA	Conventional 2-D	Proposed 2-D
I = 6 A	Avg T_q (Nm)	0.136	0.149	0.135
	Tq ripple (%)	2.92	0.51	3.25
I = 10A	Avg T_q (Nm)	0.215	0.248	0.212
	Tq ripple (%)	11.19	1.07	13.18

Table 4. Computational cost and mesh comparison for torque analysis single point.

Specification	Value		
	Real Time (Solve)	Num. of elements	Reduction Rate (Time)
3-D FEA	3,186 sec.	114,469	-
Conventional 2-D	8 sec.	31,045	99.7%
Proposed 2-D	9 sec.	33,264	99.7%

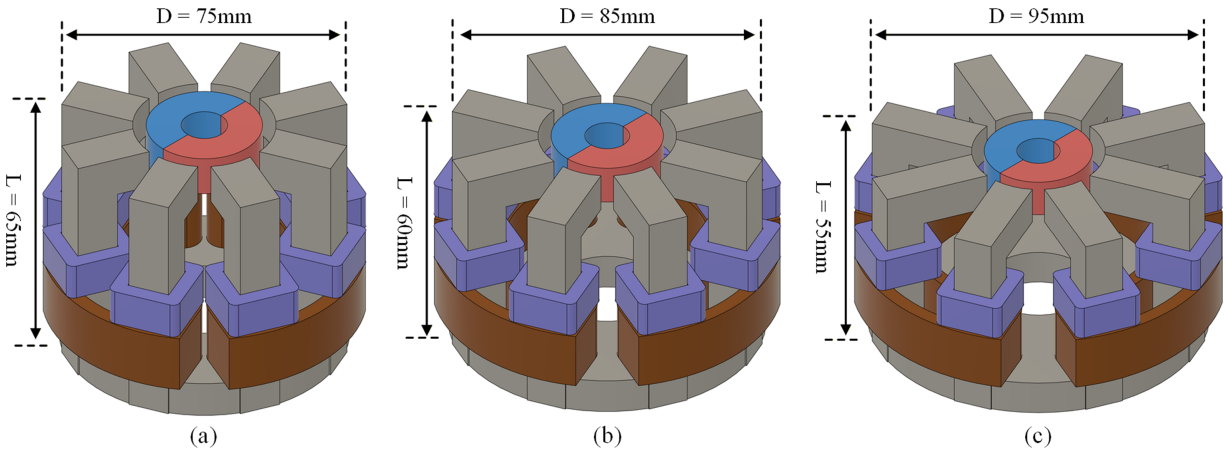


Fig. 16. (Color online) Geometric configurations of the BLMs according to K_D.

Table 5. Structural dimensions for various K_D conditions.

K_D	Specification				
	1.15	1.28	1.42	1.57	1.73
D	75 mm	80 mm	85 mm	90 mm	95 mm
L	65 mm	62.5 mm	60 mm	57.5 mm	55 mm

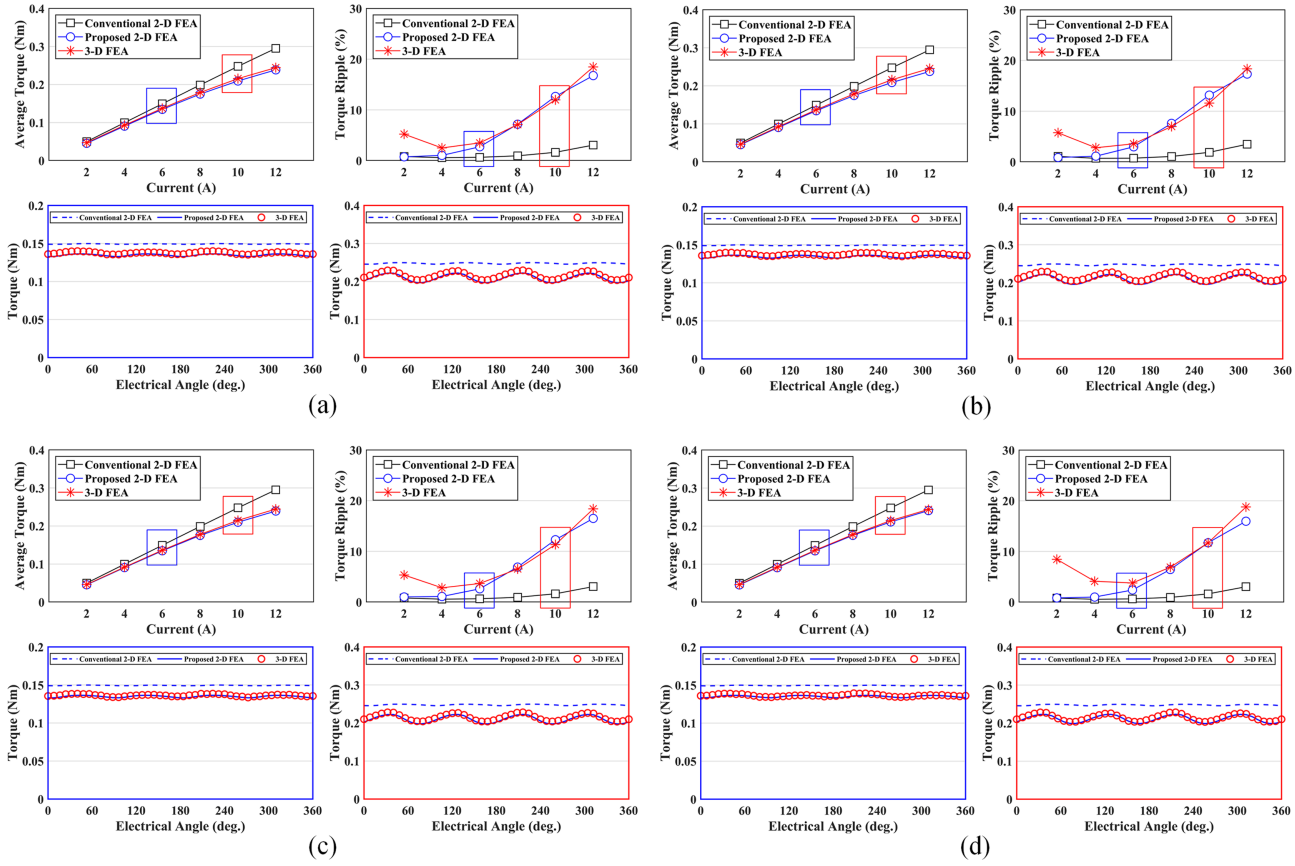


Fig. 17. (Color online) Electromagnetic torque comparison according to K_D: (a) K_D = 1.15, (b) K_D = 1.28, (c) K_D = 1.57, (d) K_D = 1.73.

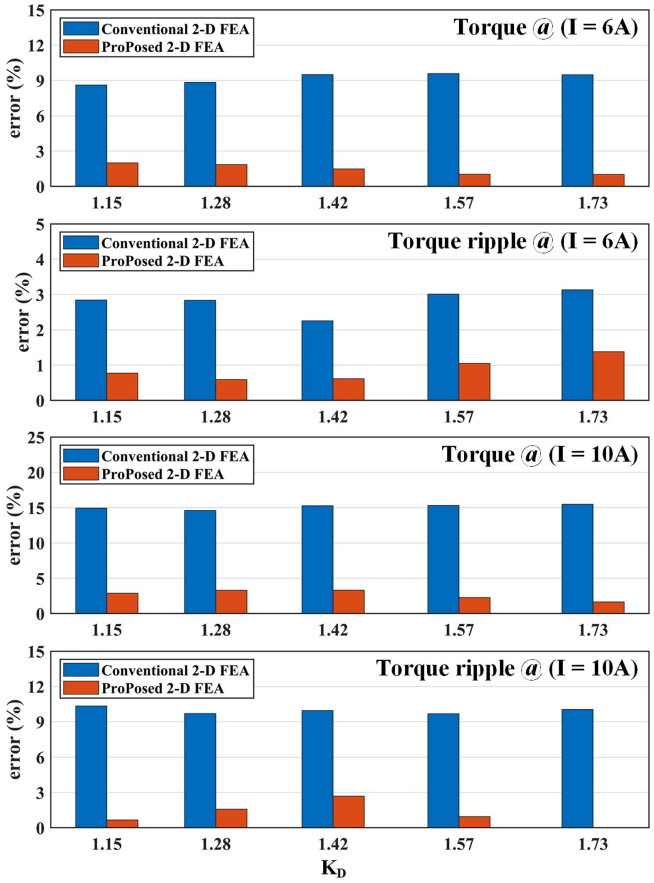


Fig. 18. (Color online) Relative error rates of average torque and torque ripple relative to 3-D FEA under current condition.

specifications of D and L, where the ratio constant is defined as $K_D = D/L$. Variations in K_D alter the balance between axial and radial flux leakage within the BLM, directly influencing its overall electromagnetic performance. Fig. 17 presents the electromagnetic torque analysis results under varying K_D conditions. Fig. 18 evaluates the relative error rates of the 2-D analysis methods compared to the 3-D FEA benchmark under rated and maximum current conditions as a function of K_D. Under the rated current condition, the proposed 2-D method demonstrates high predictive accuracy, exhibiting a maximum average torque error of 2.0% and a maximum torque ripple error of 1.38%. Under the maximum current condition, the maximum errors for average torque and torque ripple are 3.32% and 2.70%, respectively. These results confirm the robust reliability of the proposed equivalent analysis method across a wide range of diameter-to-length ratios.

Fig. 19 shows the geometric models configured to analyze performance based on the stator tooth width (W) and thickness (T). Table 6 lists the detailed dimensional parameters of W and T, where the ratio constant is denoted as $K_W = W/T$. Fig. 20 displays the electromagnetic torque analysis results under different K_W conditions. Fig. 21 illustrates the relative error rates of the 2-D analysis methods evaluated against the 3-D FEA benchmark under rated and maximum current conditions as a function of K_W. For the proposed 2-D method, the maximum errors under the rated current condition are 1.63% for average torque and 0.62% for torque ripple. Under the maximum

Table 6. Structural dimensions for various K_W conditions.

K_W	Specification				
	0.82	0.91	1.00	1.09	1.18
W	9 mm	10 mm	11 mm	12 mm	13 mm
T	11 mm	11 mm	11 mm	11 mm	11 mm

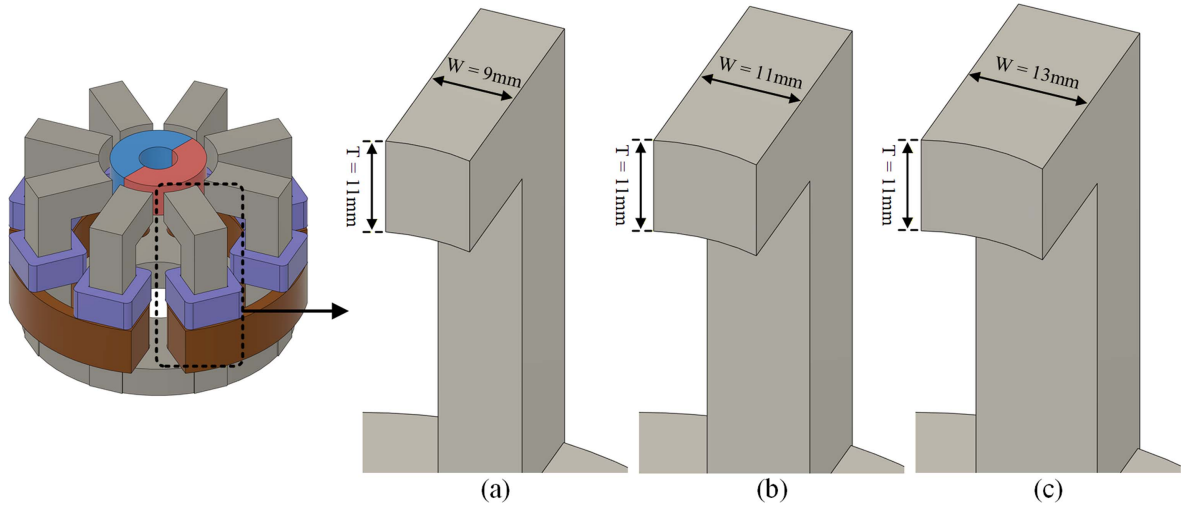


Fig. 19. (Color online) Geometric configurations of the BLMs according to K_W.

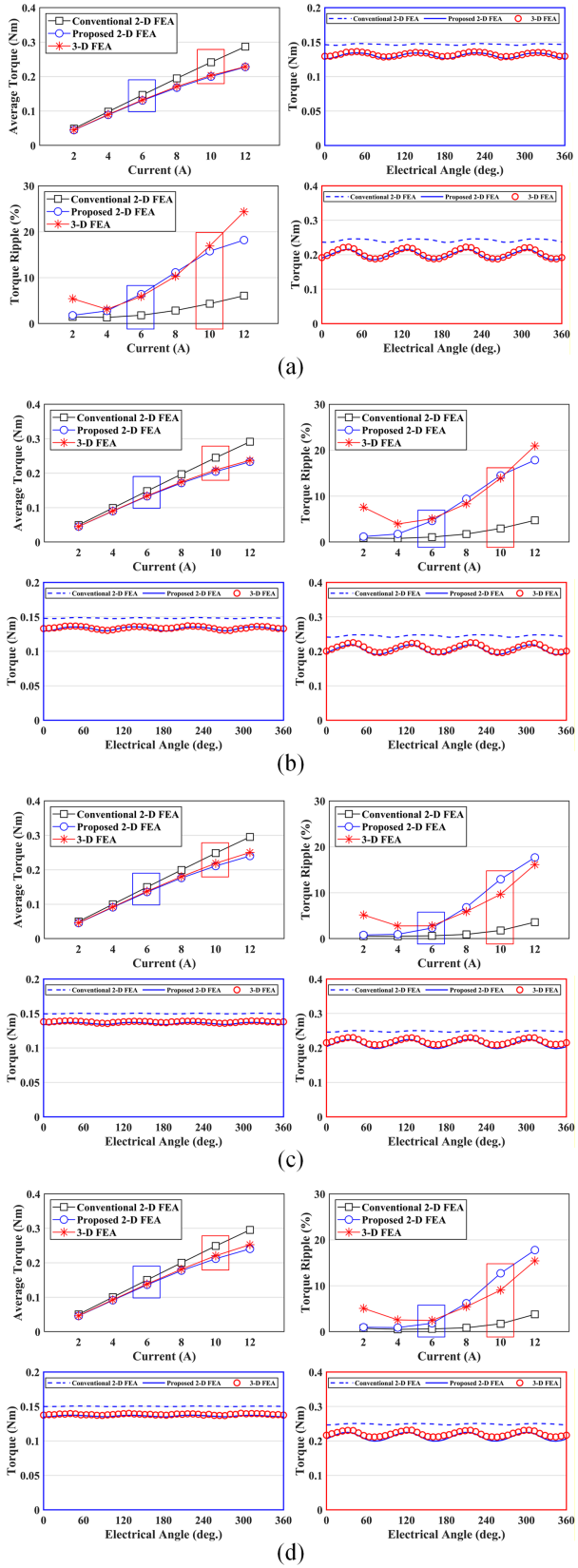


Fig. 20. (Color online) Electromagnetic torque comparison according to K_W: (a) K_W = 0.82, (b) K_W = 0.91, (c) K_W = 1.09, (d) K_W = 1.18.

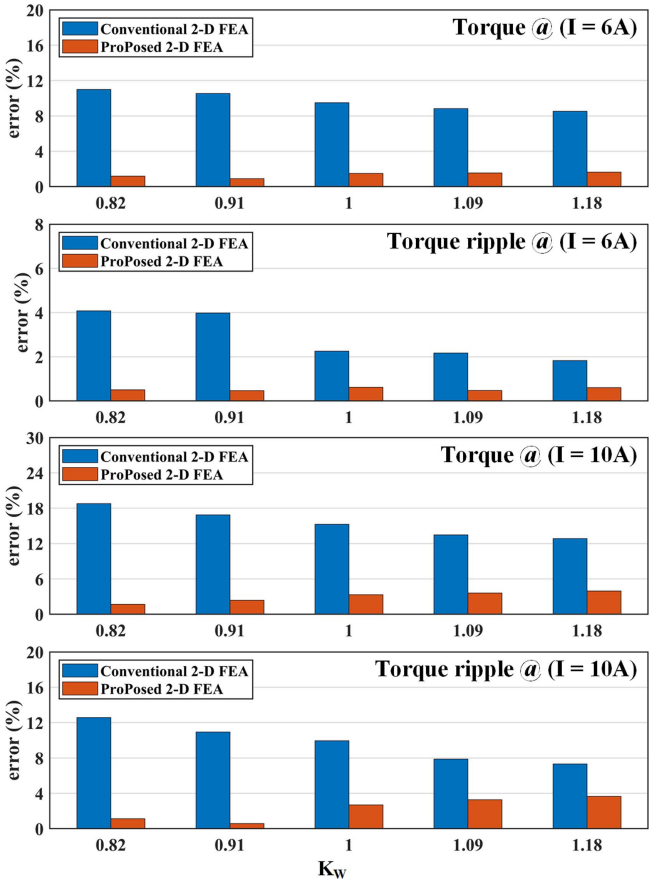


Fig. 21. (Color online) Relative error rates of average torque and torque ripple relative to 3-D FEA under current condition.

current condition, the maximum errors remain low at 3.96% for average torque and 3.66% for torque ripple. This confirms the high precision and general applicability of the proposed modeling method regardless of variations in tooth width-to-thickness ratios.

4. Conclusion

In this paper, a novel 2-D equivalent analysis model incorporating 3-D axial and radial flux leakage effects was proposed for BLMs. To overcome the inherent limitations of conventional 2-D FEA in capturing complex 3-D flux leakage paths arising from the stator's bent-teeth topology and coil layout, the overall analysis domain was discretized into 15 distinct sub-regions. Explicit formulations for region-specific permeance factors were derived and applied to adjust the relative permeability within the 2-D FEA framework, enabling precise modeling of 3-D leakage phenomena while retaining 2-D computational efficiency. The predictive accuracy and reliability of the proposed method were comprehensively validated against conven-

tional 2-D FEA and 3-D FEA benchmark results. Under the no-load condition, the proposed 2-D equivalent model significantly improved back-EMF estimation accuracy, reducing the relative error against 3-D FEA from 8.68% (conventional 2-D) to 1.42%. Under loaded conditions, the proposed model successfully reproduced electromagnetic torque magnitudes and waveform profiles, demonstrating high consistency with 3-D FEA results across both rated and maximum operating current ranges. Furthermore, parametric sensitivity evaluations across varying outer diameter-to-length ratios (K_D) and tooth width-to-thickness ratios (K_W) confirmed the general applicability and robustness of the proposed approach. Under the rated current condition, maximum errors for average torque and torque ripple remained below 2.0% and 1.38% across K_D variations, and below 1.63% and 0.62% across K_W variations. Even under the maximum current condition, maximum errors were maintained within 3.96%. Consequently, the proposed 2-D equivalent modeling method provides high accuracy with a significantly lower computational load compared to time-consuming 3-D FEA, offering high practical utility for rapid optimization and preliminary design of the BLMs.

Appendix

$$r_k = \frac{r_{si} + (k-1)(r_{so} - r_{si})}{k_a}$$

$$H_k^a = r_{k+1} - r_k$$

$$H_k^r = \frac{t_b - 0.5t_a - t_c}{k_r}$$

$$H_k^m = \pi(r_{mo} + r_{mi})$$

$$W_{sk}^a = \frac{\pi(r_{k+1} + r_k)}{N_s}$$

$$W_{sk}^{r(r_c,r_i,r_o)} = 2\pi \frac{r_{(r_c,r_i,r_o)}}{N_s}$$

$$W_{sk}^m = r_{mo} - r_{mi}$$

$$W_{ok}^a = (r_{k+1} + r_k)\left[\frac{\pi}{N_s} - \sin^{-1}\left(\frac{w_a}{r_{k+1} + r_k}\right)\right]$$

$$W_{ok}^{r(r_c,r_i,r_o)} = 2r_{(r_c,r_i,r_o)}\left[\frac{\pi}{N_s} - \sin^{-1}\left(0.5\frac{w_a}{r_{(r_c,r_i,r_o)}}\right)\right]$$

$$r_{yki} = r_{si} + l_a + t_b - 0.5(l_b + t_a + t_c)$$

$$r_{yko} = \sqrt{\frac{(r_{so}^2 - r_{yi}^2)t_c + r_{yki}^2 t_a}{4t_a}}$$

$$t_{yk} = r_{yko} - r_{yki}$$

Acknowledgment

This research was financially supported by the Ministry of Trade, Industry and Resources (MOTIR, Republic of Korea) under the "Electronic Components Industry Technology Development Program (RS-2026-25523851)" supervised by the Korea Planning and Evaluation Institute of Industrial Technology (KEIT) and the Korea Institute of Industrial Technology (KITECH) internal project (JK260002, Development of All-Diamond CMOS Technology based on a smart Lab).

References

[1] A. Chiba, T. Fukao, O. Ichikawa, M. Oshima, M. Takemoto, and D. G. Dorrell, Magnetic Bearings and Bearingless Drives, Newnes, (Elsevier), London (2005) pp. 1-15.
[2] T. Nussbaumer, P. Karutz, F. Zurcher, and J. K. Kolar, IEEE Trans. Ind. Appl. **47**, 754 (2011).
[3] H. Zhu, and F. Li, IEEE Trans. Appl. Supercond. **26**, 5202804 (2016).
[4] W. Gruber, W. Amrhein, and M. Haslmayr, IEEE Trans. Ind. Appl. **45**, 1301 (2009).
[5] R. Yang, Z. He, N. Sugita, and T. Shinshi, IEEE Access **11**, 24353 (2023).
[6] R. Puentener, M. Schuck, D. Steinert, T. Nussbaumer, and J. W. Kolar, IEEE/ASME Trans. Mech. **23**, 2963 (2018).
[7] T. Holenstein, M Schuck, and J. W. Kolar, IEEE Ind. Elect. Society **1**, 184 (2020).
[8] H. C. Roters, Electromagnetic Devices, John Wiley & Sons, New York (1941) pp. 116-150.
[9] Y. Chen, Z. Q. Zhu, and D. Howe, IEEE Trans. Ind. Appl. **44**, 1701 (2008).
[10] J. W. Jung, H. I. Park, J. P. Hong, and B. H. Lee, IEEE Trans. Magn. **53**, 8208104 (2017).
[11] J. W. Jung, M. S. Lim, J. P. Hong, and B. H. Lee, IEEE Trans. Magn. **54**, 8200904 (2018).
[12] J. W. Jung, IEEE Trans. Magn. Transp. Elecgtrif. **10**, 3438 (2024).
[13] B. H. Lee, H. I. Parck, and J. W. Jung, J. Electr Eng. Technol. **13**, 2284 (2018).